Landslides manuscript No.
(will be inserted by the editor)

Effects of grain size on subaerial granular landslides and resulting impulse waves: experiment and multi-phase flow simulation

Cheng-Hsien Lee · Zhenhua Huang

Received: date / Accepted: date

Abstract Subaerial landslides falling into a large body of water can generate large impulse waves (tsunamis). The wave generation by subaerial landslides involves sediment, water and air, and thus multi-phase flow models are most suitable for simulating the processes involved. This paper reports a laboratory and numerical study of impulse waves generated by subaerial landslides, with a focus on grain size effects. Four different grain sizes were examined in this study, ranging from fine sand to very coarse sand. A multi-phase flow model was used to perform the numerical simulations of the laboratory experiment. Both measured and simulated results have shown that the speed of the granular front and the height of the impulse wave increase with decreasing grains size. Possible explanations for the effects of grain size on the landslide process and the resulting waves are discussed.

Keywords multiphase flows · subaerial landslides · tsunamis · water waves

1 Introduction

Landslides are slope failures, which can be caused by many factors such as earthquakes and weak geological layers. Landslides can be classified as sub-

C.-H. Lee
Department of Marine Environment and Engineering, National Sun Yat-sen University, Kaohsiung 80424 Taiwan.
Tel.: +886-7-5252000 Ext. 5073
Fax: +886-7-5255060
E-mail: kethenlee@gmail.com

Z. Huang
Department of Ocean and Resources Engineering, School of Ocean and Earth Science and Technology, University of Hawaii at Manoa, Honolulu HI 96822 USA.
Tel.: +1-808-856-8100
Fax: +1-808-956-3498
E-mail: zhenhua@hawaii.edu

aerial, submarine and transitional landslides, and all three types of landslides can generate impulse waves or tsunamis (Løvholt et al., 2015; Pilvar et al., 2019). Even though landslide-generated tsunamis are rarer compared to other types of tsunamis (Cheng et al., 2020), they can be extreme dangerous compared to the tsunamis generated by submarine earthquakes or volcanic eruptions. In particular, subaerial landslides falling into lakes (Evans, 1989), reservoirs (Huang et al., 2012) or bays (Müller, 1964) can generate very large impulse waves (also called megatsunamis). For example, the 1958 Lituya Bay tsunami resulted in a run-up height of 524 m and destructed the forest on the mountain slope over a total area of 10 km^2 (Miller, 1960).

In existing experimental studies, subaerial landslides were usually modeled using either rigid blocks (Noda, 1970; Kamphuis and Bowering, 1972; Walder et al., 2003; Heller and Spinneken, 2013, 2015) or granular assemblies (Fritz et al., 2003, 2004; Zweifel et al., 2006; Heller and Hager, 2010; Viroulet et al., 2013b; Huang et al., 2014; Lindstrøm, 2016; Evers et al., 2019; Pilvar et al., 2019; Bougouin et al., 2020; Robbe-Saule et al., 2021). Existing experimental studies of impulse waves generated by subaerial landslides have shown that the near-field waves generated by rigid blocks (e.g., Heller and Spinneken, 2013) and granular assemblies (e.g., Fritz et al., 2003) share some common features: both are characterized by a leading peak, followed by several trailing waves. The near-field impulse waves may transform eventually into nonlinear oscillatory waves, transitional waves, solitary-like waves, or dissipative transient bores in the far field (Noda, 1970; Fritz et al., 2004). However, rigid blocks can generate larger waves compared to granular assemblies (Lindstrøm, 2016). It has been found that the height of the impulse waves depends primarily on the following dimensionless numbers: impact Froude number (defined by the slide speed at impact and the shallow water wave speed), dimensionless slide volume, and dimensionless slide thickness—these conclusions hold regardless of whether the subaerial landslides are modeled by block slides (Kamphuis and Bowering, 1972) or granular assemblies (Fritz et al., 2004; Zweifel et al., 2006). Other factors such as the peak ground acceleration (Wang et al., 2020) may also affect the impulse waves generated by a subaerial landslide.

Most recent experimental studies of subaerial landslides have used granular assemblies, but focused on larger particles, with the median diameter D_{50} ranging from 0.8 mm to 13.7 mm. The exception is Bougouin et al. (2020), who used non-natural particles with the smallest particles having a diameter of 0.065 mm. Two major mechanisms used to release the granular assemblies are vertical sliding gates and flapping gates. Even though vertical sliding gates have been used for most particle sizes (0.065 mm to 8.0 mm), the flapping gates have been used mainly for larger particles ($D_{50} > 4.0$ mm). A summary of representative experimental studies of subaerial landslides are given in Table 1, where the column STA indicates if the granular grains are stationary (STA) or moving at the time they are released. It can been seen from Table 1 that all these experimental studies did not report the uncertainty in the measured thickness of the granular front (ϵ_s) or the uncertainty in the measured height of the impulse waves (ϵ_H), except for McFall et al. (2016) and McFall et al. (2016)

Table 1: Summary of representative experimental studies on subaerial landslide-tsunamis

Author	Release mechanism	D_{50} (mm)	3D/2D	ϵ_s	ϵ_H	STA
Fritz et al. (2003)	Flapping gate	4.0	2D	-	-	No
Fritz et al. (2004)	Flapping gate	4.0	2D	-	-	No
Zweifel et al. (2006)	Flapping gate	4.0	2D	-	-	No
Heller and Hager (2010)	Flapping gate	2.0-8.0	2D	-	-	No
Viroulet et al. (2013b)	Vertical sliding gate	1.5	2D	-	-	Yes
Huang et al. (2014)	Vertical sliding gate	5.0-100	3D	-	-	Yes
Lindstrøm (2016)(#)	-	0.3-2.5	2D	-	-	Yes
McFall and Fritz (2016)	Flapping gate	13.7	3D	4% (*)	-	No
Zitti et al. (2016)(#)	-	9.0	2D	-	-	Yes
Mulligan and Take (2017)	Flapping gate	3.0	2D	-	-	Yes
McFall et al. (2018)	Flapping gate	13.70	3D	4% (*)	-	No
Evers et al. (2019)	Flapping gate	8.0	3D	-	-	No
Kim et al. (2019)	Flapping gate	13.7	3D	-	-	No
Pilvar et al. (2019)	Vertical sliding gate	0.8-1.0	2D	-	-	Yes
Bougouin et al. (2020)	Vertical sliding gate	0.065	2D	-	-	Yes
Huang et al. (2020)	Vertical sliding gate	2.0-5.0	2D	-	-	Yes
Robbe-Saule et al. (2021)	Vertical sliding gate	1.0-8.0	2D	-	-	Yes

(*) The thickness of the granular front was measured before it entered the water.
(#) Lindstrøm (2016) and Zitti et al. (2016) did not describe what release mechanism were used in their experiments.

who reported a 4% uncertainty in the measured thickness of the granular front before the front entered the water.

Mohammed and Fritz (2012) found that three-dimensional (3D) landslides were less efficient than two-dimensional (2D) landslides in terms of generating impulse waves. McFall and Fritz (2016) reported the deformation of 3D landslides and the waves generated, which can be used for validating 3D numerical models. Additionally, edge waves have also been observed in some 3D experiments of landslide-generated waves (Di Risio et al., 2009; Heller and Spinneken, 2015; Bellotti and Romano, 2017). The increased 3D deformation of landslides (McFall and Fritz, 2016) and the spatial spreading of wave energy (Ruffini et al., 2019) result in smaller waves in 3D than in 2D.

Most numerical models used in the literature to study impulse waves generated by subaerial landslides treat the landslide process and the hydrodynamics with an impermeable interface between the slide and the water (e.g., Løvholt et al., 2015; Kim et al., 2019), preventing the study of phenomena such as the penetration of water into dry sediment and the suspension of sediment. The hydrodynamic equations in these models belong broadly to the following two groups: (i) depth-resolving equations such as Navier-Stokes equations, which can be solved using methods such as traditional computational fluid dynamics (CFD) (Liu et al., 2005; Abadie et al., 2012; Ma et al., 2015; Kim et al., 2019; Chen et al., 2020; Romano et al., 2020; Rauter et al., 2021) and smooth particle hydrodynamics (SPH) (Vacondio et al., 2013; Shi et al., 2016), and (ii) depth-averaged equations such as shallow-water equations (Yavari-Ramshe and Ataie-Ashtiani, 2015) or Boussinesq equations (Lynett and Liu, 2005). The waves generated by subaerial landslides in these models are usually handled by one of the following methods considering landslides with a single-phase

motion: (i) simply treating the landslide as a rigid block whose motion is specified by an empirical equation (Liu et al., 2005; Lynett and Liu, 2005), (ii) solving one-layer depth-averaged equations such as the Savage-Hutter model to describe the motion and deformation of the sliding mass (Ma et al., 2015), or (iii) treating the released granular assemblies as Newtonian fluids (Abadie et al., 2012; Kim et al., 2019). Kim et al. (2019) simulated their experiments using TSUNAMI3D and FLOW3D—both TSUNAMI3D and FLOW3D simulations describe the landslide material as an incompressible Newtonian fluid.

Real-world landslides and the resulting impulse waves are multi-phase flow phenomena, of which particle-fluid interactions and particle-particle interactions all affect the landslide process and the resulting waves, and there will be mixing between the sediment phase and the fluid phase during the wave generation process. Only a limited number of multi-phase flow simulations of the impulse waves generated by subaerial landslides (Si et al., 2018; Lee and Huang, 2021) have been reported in the literature. The performance of the existing models varies. Lee and Huang (2021) showed that multi-phase models using the present formulation can capture the shape of the landslide front better than Si et al. (2018). In terms of the difference between the measured and simulated peak amplitudes, multi-phase flow models perform better than both TSUNAMI3D and FLOW3D.

In addition to the multi-phase flow models used by Si et al. (2018) and Lee and Huang (2021), Zhao et al. (2016) considered particle-fluid interactions and particle-particle interactions by a coupled DEM-CFD approach. The difference between the model of Zhao et al. (2016) and the models of Si et al. (2018) and Lee and Huang (2021) is that the former uses a Lagrangian approach for the sediment phase while the latter use an Eulerian approach for the sediment phase (both used the Eulerian approach for the fluid phase).

Existing studies did not investigate the effect of grain size on the characteristics of the impulse waves for granular slides of small particles. Most existing experimental and numerical studies of impulse waves generated by subaerial landslides focused on larger particles ($D_{50} > 0.8\,\mathrm{mm}$), except for Bougouin et al. (2020), who used artificial particles with the smallest particles having a diameter of 0.065 mm. Previous experimental studies (Heller and Hager, 2010; Lindstrøm, 2016; Robbe-Saule et al., 2021) have found that the effect of the particle size is insignificant when the diameter is larger than 1 mm. The lack of numerical simulations of fine sand is largely related to the lack of high-quality experimental data for model verification and validation: (a) fine sands can be easily suspended by the flow, which makes the determination of the sand-water interface difficult and (b) the motion of the fine sand is sensitive to minor changes in the flow field; both increase the uncertainty in the determination of the water-sediment interface. The empirical formula of Huang et al. (2014) imply that a larger particle size might result in a larger wave; however, their experiment did not isolate the effects of the particle size. They changed the particle size, the location of the granular assembly and bed slope at the same time in their experiment.

Theoretically, the wave height depends on the water volume displaced by a landslide falling into the water (Viroulet et al., 2013a). Since the permeability of a granular material, which can affect the amount of water displaced, decreases with decreasing particle size (Das, 2013), it may be hypothesized that smaller particles may displace more water and generate larger waves. To resolve the controversy in the literature over the effects of the particle size, this study reports our experimental and numerical studies of grain-size effects on the characteristics of subaerial landslides and resulting impulse waves.

The sudden collapse of a granular column has been widely used as an idealized model to study impulse waves generated by either submarine (Grilli et al., 2017) or subaerial (Viroulet et al., 2013b; Robbe-Saule et al., 2021) landslides. Similar to Viroulet et al. (2013b) this study uses the sudden collapse of a granular column located initially on a slope and above the water surface to model subaerial landslides.

2 Methods

The experimental and numerical methods adopted in this study are described in this section.

2.1 Experimental setup

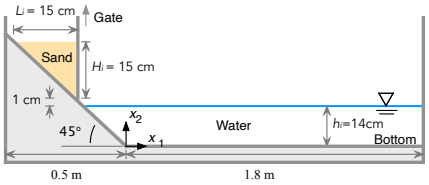

Fig. 1: Schematic diagram of the experimental setup. The numerical setup is identical to the experimental setup with the height of the computational domain being 0.4 m. The computational cells are rectangular, with the height being 4 mm in the vertical direction and the horizontal length varying from 4 mm near the inclined plane to 12 mm in the region far from the inclined plane.

Fig. 1 shows a schematic diagram of the experimental set up for 2D tests. A perspex water tank, 230-cm long, 15-cm wide and 60-cm high, was used to perform the physical tests reported in this article. To create a rough bottom condition for the granular flow, the perspex plates used to create the bottom and the slope were all coated with sand of diameter 1.29 mm. To generate a granular landslide, a sand reservoir was created on the slope by a vertical sliding gate. The vertical sliding gate release mechanism was adopted here because it is preferable over the flapping-gate release mechanism for smaller particles (see Table 1). The two lateral ends of the gate were fit into two slots

which were cut into the sidewalls of the water tank to prevent the fine sand from leaking through the narrow gaps between the gate ends and the sidewalls and to avoid possible 3D effects on the measurement of sand-water interface. The two slots were carefully aligned to ensure that the gate was perpendicular to the two sidewalls. A landslide can be generated by quickly lifting the gate. The time needed for lifting the lower end of the gate to the elevation of the initial top of the sand in the reservoir was approximately 0.1 s.

The natural sands used here all had the same density (ρ_s=2580 kg/m^3) and angle of repose ($\theta_r \approx 35°$). Four grain sizes were tested in the experiment: fine sand (F), medium sand (M), coarse sand (C), and very coarse sand (VC); their diameters are listed in Table 2. The initial volume concentration of the sand in the sand reservoir was 0.57 for all grain sizes. The room temperature during the test period was about 20°C so that the density of water ρ_f = 1000 kg/m^3 and the kinematic viscosity of water ν_f =10^{-6} m^2/s. The test conditions and the dimensions of the sand reservoir are listed in Table 2, where L_i is the length of the reservoir, H_i is the height of the sand reservoir, and h is the depth of the water body. Cases 5 and 6 in Table 2 are included to help to understand the effects of water-sand interaction on the landslide. Scale effects will be addressed in Section 4.8.

Table 2: Particle properties and test conditions.

Case	Particle type	d (mm)	L_i (cm)	H_i (cm)	h (cm)	Water body
1	Very coarse sand	1.29	15	15	14	Present
2	Coarse sand	0.66	15	15	14	Present
3	Medium sand	0.49	15	15	14	Present
4	Fine sand	0.2	15	15	14	Present
5	Very coarse sand	1.29	15	15	0	Absent
6	Fine sand	0.2	15	15	0	Absent

The toe of the sand reservoir was located 1 cm above the still water level (Fig. 1), which ensured that the sand in the reservoir was dry before lifting the gate. Two sport cameras (GoPro Hero 8) were used in the experiment: Camera A was used to record the motion of the gate and the process of a landslide and Camera B was used to record the motion of the water surface in a chosen region. The frame rate was fixed at 120 frames per second and the resolution was fixed at 1920×1080 pixels. The mode of "narrow view" was applied to avoid barrel distortion (fish-eye effect). The synchronisation of these two cameras were achieved by using a smart remote control.

Different shot angles were investigated and a low-angle camera shot was adopted because this allows for the nearest and farthest parts of the recorded moving surface to be well separated at any time of one wave period. Before processing the recorded images, color images were first converted into grayscale images and then the perspective distortion due to the camera shot angle were corrected using OpenCV, an open-source image processing tool (Bradski and Kaehler, 2008). The spatial resolutions of the images obtained by Camera A

and B are approximately 0.048 cm and 0.022 cm, respectively. After processing the images, the surface displacement at a specified location can be determined by the smallest intensity value along the vertical line through a specified location. All tests were repeated at least three times, and the uncertainty in the measured height of the first wave and the thickness of the granular front is described in Section 3.2.

2.2 Numerical setup

The computational domain has a height of 40 cm and the remaining dimensions are the same as in the experiment (see Fig. 1 and Table 2). The height of the computational domain is the vertical distance between the bottom of the tank and the upper boundary.

The multi-phase flow model of Lee et al. (2019) was adopted to simulate the waves generated by the subaerial landslides tested in the experiment. This model has been successfully used in the studies of submarine (Yu and Lee, 2019) and subaerial (Lee and Huang, 2021) landslides. The model is based on an Eulerian-Eulerian framework, treating the air and water as a single fluid phase with a variable density and viscosity. The sand is treated as the solid (sediment) phase. The formula of Lee and Huang (2018) was adopted to compute the particle response time τ_p, which is proportional to the particle diameter squared. For details of the governing equations, constitutive laws and model parameters, the reader is referred to Lee and Huang (2018) or Lee and Huang (2021). Mathematically, the effects of the grain size are included in the numerical model through the particle response time which quantifies the drag force between solid and fluid phases. The particle response time of Lee and Huang (2018) combines the formula of Richardson and Zaki (1954) for low-concentration regions and that of Engelund (1953) for high-concentration regions. Reducing the grain size reduces the particle response time and thus increases the drag force between the two phases. This allows the model to simulate the effects of grain size on flow resistance and the water penetration into the dry sand. The capillary force is not included in the model.

All rigid surfaces in the simulation were set to be hydraulically rough in analogy to the experiments. For the solid phase, the no-slip boundary condition was imposed at all rough surfaces according to Artoni and Santomaso (2014). For the fluid phase, the wall-function method (Ferziger and Peric, 2002) was applied at all rigid walls.

A total of 32,450 computational cells were used in all simulations reported here. The cells are rectangular, with the aspect ratios of the cells increasing from 1 (near the inclined plane) to 3 (far from the inclined plane) along the x_1 direction. The smallest time step was about 10^{-5} s in the simulations. Our simulations typically took two days for a physical time of three seconds using one thread on a workstation with two central processing units (Intel Xeon(R) Gold 6130 CPU). Based on our grid dependence tests, the wave heights obtained using cells with 4 mm and 2 mm in the x_2-direction have a difference

of 3 %, therefore, the height of the cells were fixed at 4 mm in the simulations presented herein.

2.3 Calculations of various forces and surface locations

The air-water interface is determined by water saturation $s = 0.5$. Since the concentration of sand c on the sand-fluid interface observed in the experiment is not a constant, the simulated location of the granular front is defined as the maximum x_2 on the contour line of $c = 0.1$; this is because the distance between two particles when $c = 0.1$ is less than a particle diameter for uniform distributed, spherical particles. We believe that no clear water-sand interface can be identified in the experiment when $c < 0.1$.

The free surface (air-water interface) displacement, the granular front, the drag force between the solid and fluid phases, the general buoyancy, the internal frictional force in the solid phase, and the frictional force between the sand and the slope are examined in this study. The drag force applied on the solid phase in a unit volume is

$$\vec{f_d} = c\rho_s \frac{(\vec{u}_f - \vec{u}_s)}{\tau_p}, \tag{1}$$

where ρ_s is the density of sand grain, τ_p is the particle response time, and u_f and u_s are the velocities of the fluid and solid phases, respectively. The general buoyancy applied on the solid phase in a unit volume is

$$\vec{f_b} = -c\nabla p_f, \tag{2}$$

where p_f is the pressure of the fluid phase. Basically $\vec{f_b}$ is the inertia force acting on all grains in a unit volume by the unsteady ambient fluid, and thus is similar to the buoyancy which is related to the gravitational acceleration. The terminology of "general buoyancy" has been used by Ouriemi et al. (2009).

The total drag force, the total general buoyancy, and the total frictional force experienced by the sediment phase are

$$\vec{F_d} = \int\int\int_{c>0} \vec{f_d}\,\mathrm{d}V, \tag{3}$$

$$\vec{F_b} = \int\int\int_{c>0} \vec{f_b}\,\mathrm{d}V, \tag{4}$$

and

$$\vec{F_f} = \int\int\int_{c>0} \nabla\cdot\left(c\bar{\bar{T}}_s\right)\mathrm{d}V, \tag{5}$$

where $\bar{\bar{T}}_s$ is the stress tensor for the solid phase and $\mathrm{d}V$ is the volume element. Since the region occupied by $c > 0$ is the entire computational domain, an application of the divergence theorem to Eq. (5) gives

$$\vec{F_f} = \int\int\int_{c>0} \nabla\cdot\left(c\bar{\bar{T}}_s\right)\mathrm{d}V = \int\int_S \left(c\bar{\bar{T}}_s\cdot\vec{n}\right)\mathrm{d}A, \tag{6}$$

where $\mathrm{d}A$ is the surface element with a unit normal vector $\vec{n}$. The surface S consists of the surfaces bounding the computational domain: the surface of the slope S_{slope}, and the surface of the bottom of the water reservoir, the surfaces of the two ends of the tank, and the ceiling of the computational domain. The frictional force experienced by the sand on the ceiling of the computational domain is zero because of the absence of the sand in the air. The frictional force that the sand experiences on the surface of each end of the tank is also negligible because of the small concentration there. Before the sand touches the bottom of the water reservoir, the total frictional force in Eq. (5) is approximately equal to the total frictional force that the sand receives from the surface of the slope, i.e.,

$$\vec{F}_f \approx \int\int_{S_{\mathrm{slope}}} \left(c\bar{\bar{T}}_s \cdot \vec{n}\right) \mathrm{d}A, \tag{7}$$

which is dominated by the component tangential to the slope.

The total forces defined by Eqs. (3)-(5) can be normalized by the total weight of the sand F_g

$$F_g = \int_{c>0} gc\rho_s \,\mathrm{d}V, \tag{8}$$

where g is the gravitational acceleration. The dimensionless forces are denoted by a subscript asterisk (*). F_g is equal to the initial weight of the sand in the sand reservoir. The corresponding dimensionless total forces is denoted by an asterisk hereafter.

3 Results

3.1 Definitions of important surfaces and thicknesses

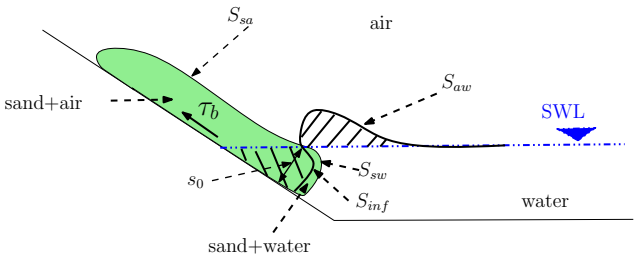

Fig. 2: Definition sketch illustrating the displacement of water by the sliding sand and the penetration of water into the sand. The region between S_{inf} and S_{sw} is occupied by the wet sand.

Fig. 2 shows a definition sketch for illustrating the displacement of water by the sliding sand and the penetration of water into the dry sand. The initial still

water level prior to the landslide is denote by SWL. Due to the penetration of water into the sand and the suspension of the sand, the sand is broadly divided into two regions: the dry sand region and the wet sand region. The dry sand is a mixture of air and sand, marked as "sand+air"; the wet sand is a mixture of water and sand, marked as "sand+water" in the sketch. The interface between the dry and wet sand indicates the extent of water penetration and is denoted by S_{inf}. The air-water interface outside the sand is denoted by S_{aw}, the sand-water interface by S_{sw}, the sand-air interface by S_{sa}. The interface between the dry and wet sand, S_{inf}, is the result of the penetration of water into the sand. The pressure at S_{inf} is affected by the local water motion and influences the air flow inside the sand through the dynamic boundary condition at S_{inf}. The maximum distance of S_{inf} to the surface of the slope is denoted by s_0, which is the thickness of the dry portion of granular front. The averaged shear stress between the sand and the slope is denoted by τ_b. The area bounded by S_{inf} and the still water level, which is related to the amount of water displaced, is marked as a shaded region in Fig. 2. The area between S_{aw} and the still water level, which is the amount of water displaced by the the sliding sand, is also marked as a shaded region.

To compare the experiments and numerical simulations, the time for the recorded images was adjusted such that the difference between the measured and simulated water surfaces of S_{aw} in the range of 0 to 0.3 m is minimized at the simulation time, say $t = 0.6$ s, in the nonlinear-least-squares sense.

3.2 Repeating tests and uncertainty in experimental results

The uncertainty in the experiment can be estimated based on the results from the repeating tests, which shows that (1) the uncertainty in the measured height of the first wave was less than 1.1 mm or 6.8% for the very coarse sand and 4.6% for the fine sand and (2) the uncertainty in the measured thickness of the submerged granular front was less than 10% for d=0.49, 0.66 and 1.2 mm, but was 30% for d=0.2 mm.

The uncertainty in the measured height of the first wave is mainly related to the operation of the release mechanism. A 6.8% uncertainty in the measured wave height is believed to be acceptable in this study. In addition to the release mechanism, the uncertainty in the thickness of the granular front is also strongly affected by (i) the suspension and diffusion of granular grains and (ii) the easiness of identifying the water-sediment interface. Both are strongly influenced by the grain size.

3.3 Description of sliding process and waves generated

Six snapshots, showing the recorded and simulated landslide and wave-generation processes for Case 1, are presented in Fig. 3, where the colored lines are contour lines used to indicate the simulated air-water, air-sand and water-sand

surfaces. The granular mass in each video-recorded image is identified by the darker area above the slope. Even though the experiment was designed to be two-dimensional, it may not be exactly two dimensional due to minor sidewall effects, inherent three-dimensional turbulent fluctuations and possible wave breaking and air entrainment (or free-surface aeration). The interface between the sand and the fluid captured by the camera is what the camera records from a given shot angle, and the shape of the granular mass in the cut-surface at the front wall for the shot angle used here. The impulse waves captured by the camera are indicated by the darker area in each image in Fig. 3, which shows the three-dimensional water surface between the two sidewalls. Each of the sharp edges between this darker area and the lighter background indicates the intersection of the air-water interface and a sidewall: the upper edge of the darker area in each image is the water-surface profile at the front wall because the camera was placed at an elevation below the still water surface in the experiment. Since the numerical simulation is two-dimensional, the simulated air-sand, water-sand and air-water interfaces should be compared with the corresponding interfaces measured at the front wall. It is remarked that the simulated air-water interface inside the sand indicates the extent of the water penetration into the sand.

Referring to the recorded fluid-sand interface in Fig. 3, the toe of the granular front has entered the water at $t \sim 0.1\,\mathrm{s}$, displacing the water above and starting the generation process of the first wave. A wavy feature develops on the recorded fluid-sand interface as the sand slides down the slope. Starting from $t = 0.4$ to $0.5\,\mathrm{s}$, two humps can be observed on the recorded fluid-sand interface: one is the granular front and the other is close to the middle section of the sliding mass. The first hump is noticeable at $t \sim 0.4\,\mathrm{s}$, touches the flat bed at a time between 0.4 and $0.5\,\mathrm{s}$, and becomes unrecognizable when it has moved onto the flat bed. The second hump is formed at a time before $t \sim 0.5\,\mathrm{s}$ and the absolute location is more or less stationary relative to the slope. It is remarked that due to the limited length of the granular slide here, it is difficult to tell if the wavy feature observed here is a long wave observed by Forterre and Pouliquen (2003). At $t \sim 1.2\,\mathrm{s}$, the granular front no longer has noticeable motion, but a portion of the sand on the slope continues to slide down slowly. The crest of the first wave becomes noticeable at $t \sim 0.2\,\mathrm{s}$. As the sand continues to slide on the slope, the first-wave crest grows and eventually leaves the granular front at $t \sim 0.4\,\mathrm{s}$; at $t \sim 0.6\,\mathrm{s}$, the crest of the second wave can be observed next to the second hump, and at $t \sim 1.2\,\mathrm{s}$, the second wave has left the second hump. The flow separation from the granular front is manifested by the sporadic particles suspended in water on the lee side of the granular front at $t > 0.4\,\mathrm{s}$, indicating the existence of a low-concentration region in the vicinity of the granular front.

Referring to the simulated fluid-sand and air-water interfaces in Fig. 3, the numerical simulation captures the key features of the evolution of fluid-sand interface and the waves generated, especially the key features of the two humps and the heights of the impulse waves. From $t = 0.2$ to $0.5\,\mathrm{s}$, the distance between the two contour lines of $c = 0.1$ and $c = 0.5$ near the granular front

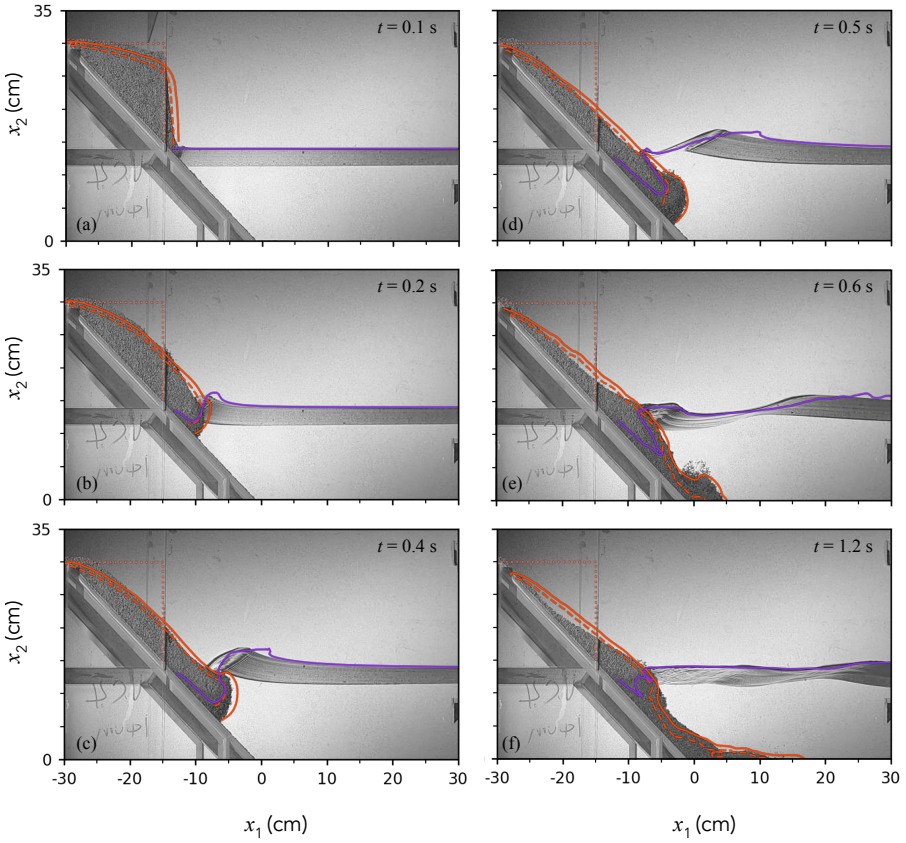

Fig. 3: Snapshots of the observed (Camera A) and simulated landslide processes and waves at t = 0.1, 0.2, 0.4, 0.5, 0.6, and 1.2 s (a)-(f) for Case 1. The simulated contour lines of $c = 0.1$ (solid orange lines) and of $c = 0.5$ (dashed orange lines) are included for comparison with the observed fluid-sand interface. The air-water interface in the numerical results is defined by $s = 0.5$ (the solid purple line). The upper edge between the darker area and the lighter background in the region occupied by the water is the air-water interface at the front wall. The dotted orange line on each plot outlines the initial shape of the sand pile on the slope.

increases, indicating a dilution of the sand due to the response of the sand to the local water motion. It can be observed that the locations of the simulated and measured crests of the first wave differ by about 8 cm: the simulated wave crest moves slightly faster than the measured one. If $\sqrt{gh}$ is used, with $h \sim 0.145$ m being the local water depth, to provide a rough estimation of the speed of the first wave, this 8 cm-difference in crest locations is equivalent roughly to a difference of 0.067 s in the arrival time of the first crest in Fig. 4. This 0.067 s-difference in the arrival time is slightly less than the time required to complete the gate lifting (about 0.1 s).

Fig. 4 shows the measured and simulated free surface displacements at $x_1 = 0.3$ and 0.4 m (measured from the toe of the slope) for Case 1. To indicate the uncertainty in the measured surface displacements at the two locations, three repeating tests are shown. Our simulated surface displacements can match the measured ones reasonably well at both locations, except that the simulated first wave has a spike near the crest at $x = 0.3$ m and a slight earlier arrive time. The spike is possibly due to the splashing water in the simulation which was not captured by the recorded images. The difference in the arrival times is about 0.07 to 0.08 s, which is caused mainly by the different release mechanisms used in the experiment and the simulation. It can also be observed that, as the waves propagate from $x_1 = 0.3$ to 0.4 m, the nonlinear wave dispersion causes the period of the first wave to increase slightly, the amplitude of the first wave to decrease slightly, and the amplitude of the second wave to increase slightly.

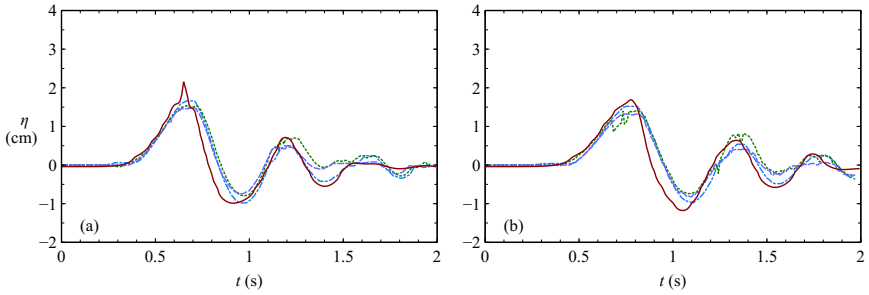

Fig. 4: Comparison between the surface displacement measured by Camera B (dashed lines) and the computed surface displacement (solid line) at (a) $x_1 = 0.3$ m and (b) $x_1 = 0.4$ m for Case 1. Three repeating tests are indicated by the three dashed lines.

Fig. 5 shows the simulated locations of the granular front and the first wave crest, and the height of the first wave for Case 1. Before the first wave leaves the granular front, the first wave is a forced wave, moving with the granular front whose speed gradually decreases due to the resistance from the water and the loss of potential energy. The first wave is initially a forced wave and then becomes a free wave after it leaves the granular flow front (Lee and Huang, 2021). The speed of a free wave is controlled by the local water depth which increases down the slope. Two critical times can be identified from Fig. 5: (i) $t_{c1} \approx 0.15$ s, a critical time at which the speed of the first wave begins to exceed the speed of the granular front and (ii) $t_{c2} \approx 0.26$ s, a critical time at which the first wave has reached its maximum height, implying that it has completely left the granular front and thus stopped receiving energy from the slide. Because of the energy dissipation and the increase of the water depth as the wave propagates, it is possible that the wave height may slightly decrease while the wave is still receiving energy from the slide.

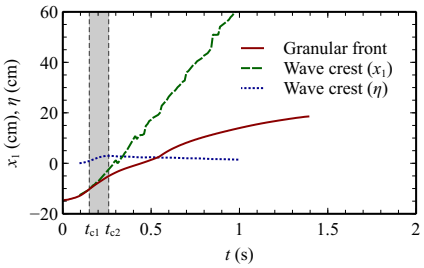

Fig. 5: The simulated height of the first wave and the positions of the granular front and the wave crest for Case 1. The shaded band indicates the time interval within which the first wave is in transition from a forced wave to a free wave. For this case, $t_{c1} \approx 0.15\,\mathrm{s}$ and $t_{c2} \approx 0.26\,\mathrm{s}$.

3.4 Overview of the tests and simulations for the four grain sizes

For each particle size, a snapshot of the sliding process at the critical time $t = t_{c2} \sim 0.26\,\mathrm{s}$ is shown in Fig. 6, where both the experimental and simulated results are included for comparison. Two contour lines ($c = 0.1$ and $c = 0.5$) are included in order to compare the simulated fluid-sand interface with the measured one. The simulated air-water interface, inside and outside the sand, is defined by $s = 0.5$. It can be observed that (i) the simulated granular front is slightly thicker than the measured one and (ii) the simulated fluid-sand and air-water interfaces are in general agreement with the measured ones for all four cases, except for some fine details: the thickness of the granular front and the arrival time of the first crest, which will be discussed in Section 4.6.

A comparison of the results of the four tests shown in Fig. 6 reveals that (i) finer sand slides slightly faster in both the experiment and the simulation, (ii) the simulated thickness of the granular front increases with reducing grain size, and (iii) the distance between the two contour lines of $c = 0.1$ and 0.5 near the granular front increases with reducing grain size, indicating that the dilution/suspension of the sand in that region is stronger for fine sand.

3.5 Effects of grain size on the sliding speed and the thicknesses of granular fronts

As stated in Section 3.4, two contour lines are included in Fig. 6 to indicate the simulated fluid-sand interface in order to compare with the experiment. The contour line of $s = 0.5$ inside the sand indicates the extent of the water penetration into the sand, which is controlled by the penetration of the water and dilution of the sand. If the sand with $c > 0.5$ can be regarded as undiluted sand, an intersection of the contour line $c = 0.5$ and the air-water interface in the sand ($s = 0.5$) indicates that the water has penetrated into the core of the undiluted sand.

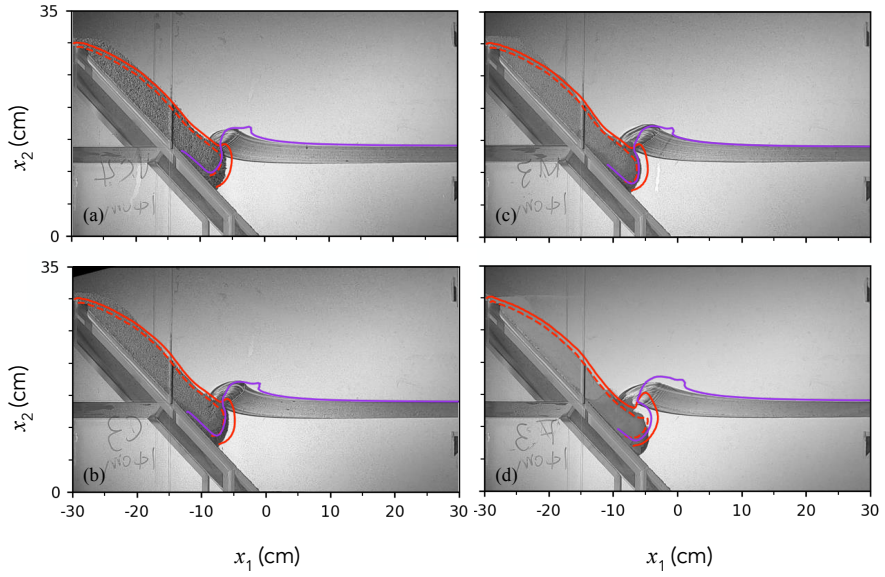

Fig. 6: Snapshots of the observed and simulated landslide process and free surface displacement at $t = 0.26$ s for Cases 1-4 (a-d). The orange dashed line is the contour line of $c = 0.5$ and the orange solid line is the contour of $c = 0.1$. The purple solid line is the air-water interface. The upper edge between the darker area and the lighter background in the region occupied by the water is the air-water interface at the front wall.

Table 3: Thicknesses describing the granular front at $t = 0.26$ s and the corresponding averaged speeds between $t = 0$ and 0.26 s

Case	d [mm]	$\delta_{\exp}$ [cm]	$\delta_{0.1}$ [cm]	$\delta_{0.5}$ [cm]	s_0 [cm]	$U_{\exp}$ [m/s]	$U_{(0.1)}$ [m/s]	$U_{(0.5)}$ [m/s]
1	1.29	4.9	5.9	4.2	5.1	0.36	0.38	0.33
2	0.66	5.5	6.1	4.2	5.1	0.38	0.39	0.37
3	0.49	5.5	6.1	3.8	5.2	0.39	0.40	0.38
4	0.20	5.5	7.5	4.7	5.9	0.43	0.46	0.39

It is the dry portion of the granular front that displaces the water and contributes to the wave generation (Fig. 2). The thickness of the dry portion of the granular front s_0 is the maximum distance between S_{inf} and the slope. The values of s_0 at $t = 0.26$ s are given in Table 3 for Cases 1-4. The local maximum distances between the slope surface and the contour lines of $c = 0.1$ and 0.5 near the granular front are denoted by $\delta_{0.1}$ and $\delta_{0.5}$, respectively, and their values determined at $t = 0.26$ s are also included in Table 3 for Cases 1-4. It can be concluded that (i) the four thicknesses listed in Table 3 generally increase with decreasing grain size, (ii) the thickness of the granular front in

the experiment δ_{exp} falls between $\delta_{0.1}$ and $\delta_{0.5}$, and (iii) the thickness of the dry portion of the granular front s_0 also falls between $\delta_{0.1}$ and $\delta_{0.5}$.

Two simulated speeds of granular front averaged over the time interval of 0 s to 0.26 s can be deduced from the instantaneous contours of $c = 0.1$ and $c = 0.5$ near the granular front, and are denoted by $U_{(0.1)}$ and $U_{(0.5)}$, respectively. The measured speed of the granular front U_{exp} can be deduced from the locations of the water-sand interface in the recorded images. Since the concentration on the sand-water interface is not constant, it is reasonable to expect that the measured slide speeds fall between $U_{(0.1)}$ and $U_{(0.5)}$, which is confirmed in Table 3. It is further showed in Table 3 that (i) the slide speed increases with decreasing grain size and (ii) $U_{(0.1)} > U_{(0.5)}$ because of the dilution/suspension of the sand.

3.6 Effects of the particle size on the height of the first wave

Fig. 4 shows that the height of the first wave is always larger than that of the second wave (see also Bougouin et al., 2020); therefore, it is desirable to understand how the grain size affects the height of the first wave. As shown in Fig. 7, both the simulated and measured heights of the first wave have the same trend: they all decrease with increasing grain size. Even though the simulated heights are larger than the measured, the difference decreases with increasing the grain size: the relative differences are 10 % for the very coarse sand and 30 % for the fine sand. As will be discussed in Section 4.6, the over-prediction of the wave height might be related to the model for the particle response time which is related to the particle settling velocity. The evaluation of the model performance is given in Section 4.7

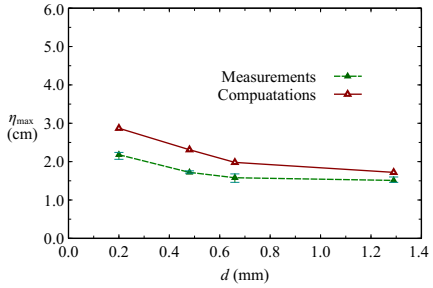

Fig. 7: Comparison between the measured and simulated wave heights η_{max} at $x_1 = 0.4$ m. The error bars represent the uncertainty of the measured heights of the first wave in three repeating tests.

3.7 Simulated fields of velocity, pressure, drag force and general buoyancy

The simulated fields of velocity, pressure, drag force and general buoyancy for the fine sand and very coarse sand are included in Figs. 8 and 9. The simulated fields for the coarse sand and medium sand are not included as they are very similar to those in Fig. 8.

3.7.1 The very coarse sand

Fig. 8 shows the following simulated quantities for Case 1 at two instants of time ($t = 0.26$ and 0.6 s): the velocity of the solid phase $\vec{u}_s$, the velocity of the fluid phase $\vec{u}_f$, the pressure of the solid phase p_s, the pressure of the fluid phase p_f, the drag force f_d, and the general buoyancy f_b. The failure line defined by $|\vec{u}_s| = 0.1$ m/s is also included in each plot.

Referring to Figs. 8(a) and 8(e), the failure line below which the sand is virtually stationary is already deeply buried in the sliding sand at $t = 0.26$ s, but the motion of the sand is mostly localized near the granular front at $t = 0.6$ s. As the sand slides down the slope, the velocity of the dry sand on the slope reduces. The maximum values of the instantaneous sediment-phase velocities on the contour lines of $c = 0.1$ and $c = 0.5$ are, respectively, 1.12 m/s and 0.82 m/s at $t = 0.26$ s (the instantaneous velocity should be larger than the averaged velocity in Table 3). In the region between the contour lines $c = 0.5$ and $c = 0.1$, it is the dilution (wet sand) and dilation (dry sand) that affect the concentration. The pressure of the solid phase is the largest in the region close to the dry-wet sand interface where $c > 0.5$.

A vortex begins forming near the granular front at $t = 0.26$ s in Figs. 8(b) and (f). The vortex moves faster than the granular front and is close to the toe of the slope at $t = 0.6$ s. The total pressure of the fluid phase is much larger near the bottom and gradually decreases toward the wet-dry sand interface. The pressure of the fluid phase at $t = 0.26$ s is generally less than 891 Pa in the dry sand.

In Figs. 8(c) and (g) the drag force between the wet sand and the water is much larger than that between the dry sand and the air. Within the wet sand, the drag force is small in the region where $c > 0.5$. For the very coarse sand studied here, the vertical component of the drag force dominant at $t = 0.26$ s.

Figs. 8(d) and (h) show that the general buoyancy experienced by the solid phase is significant only on the wet sand side of the wet-dry sand interface. This force has a tendency to be perpendicular to the wet-dry sand interface, and thus can slow down the motion of the granular front.

3.7.2 The fine sand

Fig. 9 shows the simulated results for Case 4. A comparison of Figs. 8 and 9 shows that the general patterns of the velocity and pressure fields of the solid and fluid phases are similar. However, differences can be found in the

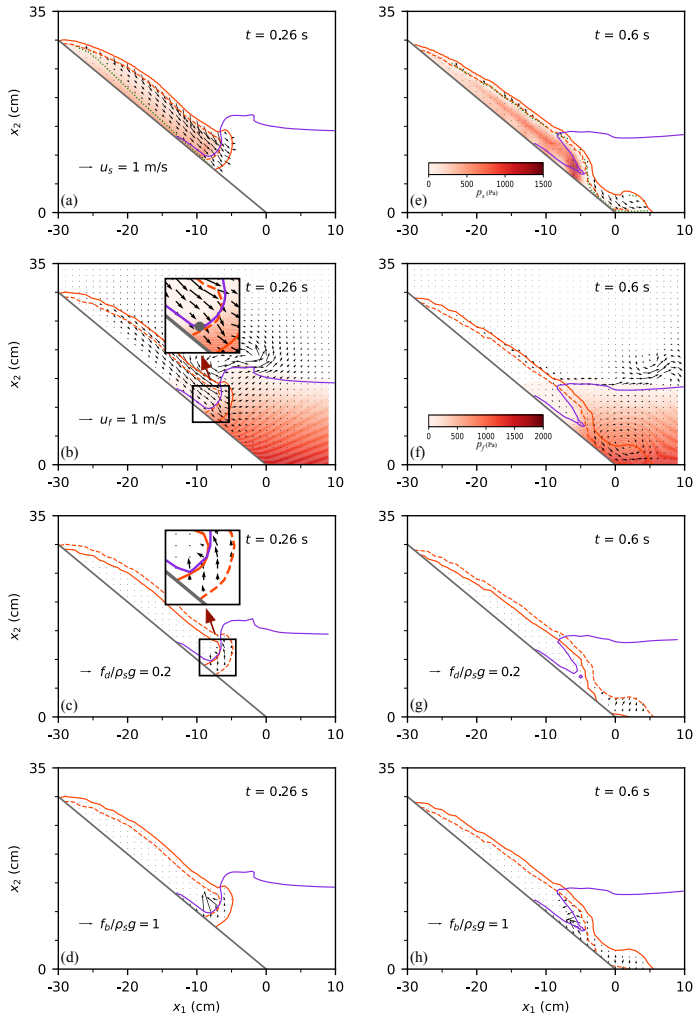

Fig. 8: Simulated fields of the following quantities at two instants of time for Case 1: (i) the solid-phase velocity and pressure (a,e), (ii) the velocity and pressure of the fluid phase (b, f), (iii) the dimensionless drag force on the solid phase (c,g), and (iv) the dimensionless buoyancy (d, h). The contour lines of $c = 0.1$ (solid lines) and of $c = 0.5$ (dashed lines) are presented. The air-water interface (purple line) is defined by $s = 0.5$. The dotted lines in panels (a) and (e) present the failure lines. The fluid-phase pressure at the point marked by • in panel (b) is 891 Pa.

magnitude of the velocity of the sand near the granular front, the general buoyancy, and the magnitude of the total pressure of the air in the dry sand.

For the fine sand, the maximum solid-phase velocities on the contour lines of $c = 0.1$ and $c = 0.5$ are, respectively, 1.16 m/s and 0.94 m/s at $t = 0.26$ s. Both are larger than the corresponding ones for the very coarse sand, mean-

ing that the fine sand slides slightly faster than the very coarse sand at this moment.

The grain size affects the pressure of the air in the sand on the dry-sand side of the wet-dry interface, which is higher in the fine sand: the maximum pressure p_f in the dry sand at $t = 0.26$ s is about 1295 Pa in Fig. 9 (b), much larger than 891 Pa in Fig. 8 (b) for the very coarse sand. The possible reason for this and its effects on the landslide process and the resulting impulse waves will be discussed in Section 4.

The grain size also affects the general buoyancy. For the very coarse sand, the general buoyancy is significant only on the wet sand side of the wet-dry interface and the direction tends to be perpendicular to the wet-dry interface at $t = 0.26$ s. For the fine sand, the general buoyancy is also significant in a larger region on the dry sand side of the wet-dry interface, and the direction of the general buoyancy has a significant vertical component at t=0.26 s; therefore, it does not provide a direct resistance to the granular flow as opposed to the direction for the very coarse sand, which is generally perpendicular to the wet-dry sand interface.

3.8 Simulated total forces experienced by the sediment phase

The dimensionless frictional force F_f^* is shown in Fig. 10 and the dimensionless buoyancy F_b^*, and the dimensionless drag force F_d^* tangential (with the subscript $_\parallel$) and perpendicular (with the subscript $_\perp$) to the slope are shown in Fig. 11 for Cases 1 to 4.

Referring to Fig. 10, after the release of the sand in the simulation, the sand first needs to go through an initial adjustment period ($t < 0.02$ s), see Appendix 5 for details. After the initial adjustment, the sand slides down first on the dry slope. Before the sand is in contact with the water, the dimensionless frictional force F_f^* is expected to be nearly the same as that in the absence of water. Both the very coarse sand and the fine sand have almost the same frictional force in the absence of the water body as shown in Appendix 5. A comparison of the frictional forces for Case 1 (very coarse sand) and Case 4 (fine sand) in Fig. 10 and those in Appendix 5 show that the water-sand interaction begins to affect the frictional force at about t=0.1 s and the water-sand interaction reduces the frictional force F_f^*, with the reduction for the fine sand being larger than those for the other three. In particular, the water-sand interaction causes the fine sand to experience a dimensionless frictional force F_f^* smaller by about 0.07 than the very coarse sand. It is interesting to note that the dimensionless frictional forces for the coarse (Case 2) and medium (Case 3) sands are similar to that for the very coarse sand.

A comparison of Fig. 11 and Fig. 10 shows that the frictional force is in general several times larger than the general buoyancy, while the general buoyancy is generally several times larger than the drag force. For each grain size, the two components of the general buoyancy ($F_{b\parallel}^*$ and $F_{b\perp}^*$) are very small before $t \sim$0.1 s and increase gradually afterward. After $t \sim$0.2 s, $F_{b\perp}^*$ decreases

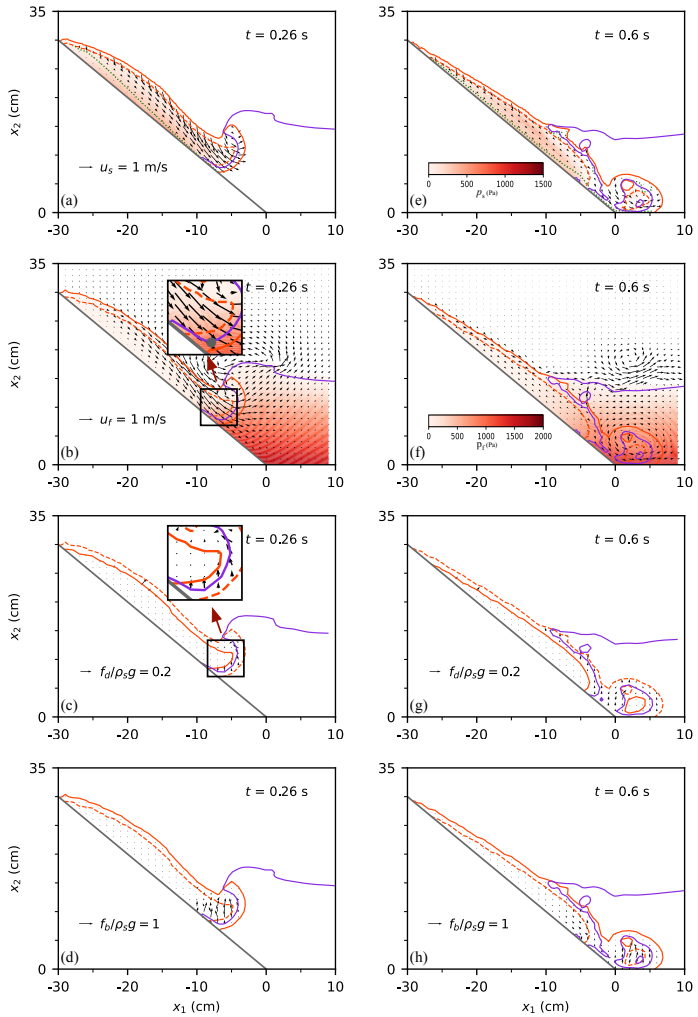

Fig. 9: Simulated fields of the following quantities at two instants of time for Case 4: (i) the solid-phase velocity and pressure (a,e), (ii) the velocity and pressure of the fluid phase (b, f), (iii) the dimensionless drag force on the solid phase (c,g), and (iv) the dimensionless buoyancy (d, h). The contour lines of $c = 0.1$ (solid lines) and of $c = 0.5$ (dashed lines) are presented. The air-water interface (purple line) is defined by $s = 0.5$. The dotted lines in panels (a) and (e) present the failure lines. The fluid-phase pressure at the point marked by • in panel (b) is 1295 Pa.

for the fine sand and medium sand, maintains almost flat for the coarse sand, and still gradually increases for the very coarse sand. The fine sand experiences more general buoyancy than the other three and the differences between the fine sand and the very coarse sand are about 0.03 for $F^*_{b\parallel}$ and about 0.07 for $F^*_{b\perp}$. For the fine sand, $F^*_{b\perp}$ is comparable to $F^*_{b\parallel}$, while for the other three,

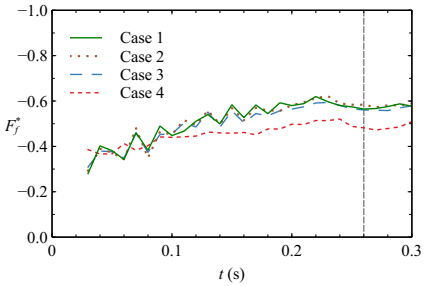

Fig. 10: Time series of the total frictional force experienced by the sand on the slope for Cases 1 to 4. The vertical dashed line at $t \sim 0.26$ s indicates the instant of time at which the first wave leaves the granular front.

$F^*_{b\perp}$ is smaller than $F^*_{b\parallel}$. It is remarked that the general buoyancy for the very coarse sand is significant only in the wet sand (see Fig. 8), but for the find sand it is significant in the dry sand (see Fig. 9). The effect of grain size on the drag force is similar to that on the general buoyancy, but the general buoyancy is several times larger than the drag force.

Physically, the frictional force between the sliding sand and the slope is proportional to the normal component of the solid-phase pressure. Therefore, it is expected that an increased $F^*_{b\perp}$ has the tendency to reduce the frictional resistance experienced by the solid phase; this is confirmed by a comparison of Figs. 11(b) and 10.

It can be concluded from this section that the presence of water can reduce the frictional force, especially for the fine sand. Although the presence of water can rise the general buoyancy and drag force, which has the tendency to slow down the motion of sand in water, the magnitudes of the buoyancy and drag are much smaller than that of the frictional force.

4 Discussion

Possible explanations are provided here for: (i) why the air pressure in the fine sand is larger than in the very coarse sand, (ii) why the fine sand slides faster than the very coarse sand, (iii) why the height of the first wave increases with decreasing grain size, and (iv) why the over-prediction of the height of the first wave increases with increasing grain size. In this section the height of the first wave is referred to as "the wave height" and the speed of the granular front on the slope is referred to as "the sliding speed". The sand in suspension with low concentrations ($c < 0.1$) will be ignored in the following.

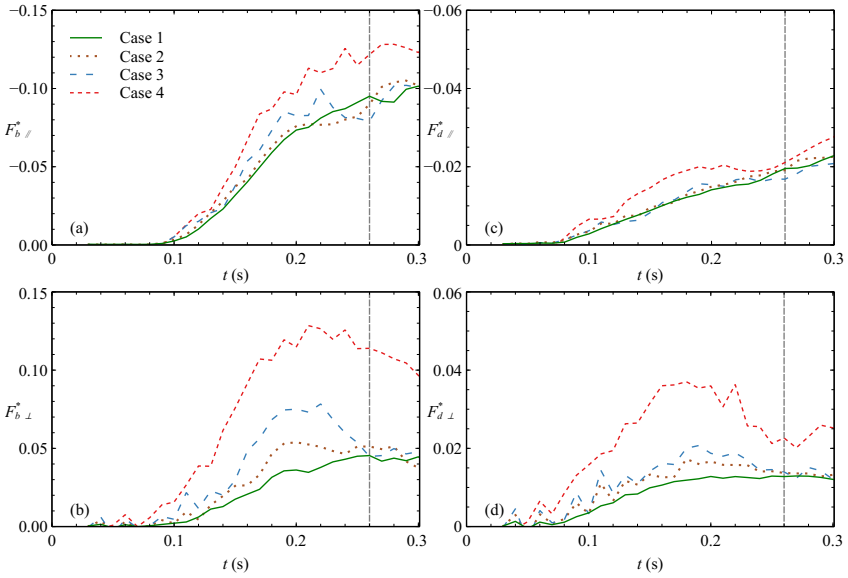

Fig. 11: (a, b) Time series of the buoyancy along and perpendicular the slope; (c, d) drag force along and perpendicular the slope. The vertical dashed line on each plot indicates the instant of time at which the first wave leaves the granular front.

4.1 Penetration of water into the sand, volume of the wet sand and volume of the displaced water

Fig. 2 shows that the volume of the water displaced by the landslide is affected by two factors for the present problem with a low drop height (the initial elevation of the slide material): (i) the volume of the wet sand (indicated in the sketch by "sand+water") and (ii) the volume of the dry sand in the region bounded by S_{inf} and the still water level (marked in the sketch as a shaded region in the sand).

The effect of the grain size on the volume of the wet sand can be understood in the following way. Assuming that the area occupied by the wet sand is formed by two separated processes: the penetration of water into the sand without suspension/dilution and the suspension/dilution of the sand without further penetration. In the first process the concentration of the sand does not change, while in the second process the dry-wet interface S_{inf} does not change. Under these assumptions, the location and the shape of the dry-wet interface S_{inf} in relation to the dry sand is determined mainly by the penetration process. Therefore, S_{inf} should be controlled mainly by the penetration process in the absence of suspension/dilution. The volume of the sand in the area bounded by S_{inf} and the still water level should decreases with increasing penetration rate, which increases with increasing grain size (Das, 2013); as a result, the thickness s_0 decreases with increasing grain size, as shown in Table 3, and the total volume of the wet sand increases with increasing penetration

rate. Therefore, the volume of the wet sand for the very coarse sand should be larger than that for the fine sand. Therefore, the volume of the wet sand is not a direct reason for the larger wave height associated with the fine sand.

For the present problem with a low drop height, the volume of the dry sand in the region bounded by S_{inf} and the still water level is approximately equal to the volume of the water displaced by the sliding sand because the volume of the wet sand is small at the time when the first wave is leaving the granular front (see Fig. 6). Therefore, according to the conservation of mass, the total volume of the water displaced by the sliding sand, which is marked as a shaded region in Fig. 2, should be approximately equal to the volume of the dry sand in the region bounded by S_{inf} and the still water level, which is proportional to s_0, the maximum distance between S_{inf} and the slope. Since s_0 is expected to increase with decreasing grain size as shown in Table 3, the volume of the dry sand in the region bounded by S_{inf} and the still water level should increase with decreasing gain size.

Hsu et al. (2002) and Higuera et al. (2014) have used the approach based on the volume-averaged Reynolds-averaged Navier–Stokes equations (VARANS) to simulate the infiltration (or water penetration into a porous media). Our model reduces to VARANS when the solid phase is stationary (Higuera et al., 2014). VARANS considers only the effects of porous media on the water-flow (one-way coupling). The present multi-phase model is a so-called "four-way couplings model", which considers the two-way coupling between fluid and particles as well as particle-particle collisions.

It is stressed here that when a problem involves a high drop height, the speed of the granular material at impact is high (Fritz et al., 2003, 2004; Zweifel et al., 2006; McFall and Fritz, 2016; McFall et al., 2018), and thus the high momentum and kinetic energy at impact also influence the volume of the displaced water. Fritz et al. (2004) found that the volume of the displaced water in this case could be much larger than that of the submerged granular material.

4.2 Air pressure in the dry sand

The higher air pressure in the fine sand, which can be seen by comparing Figs. 8 and 9, may be understood from the height of the first wave and the speed of the granular front.

The pressure on the air-water interface excluding S_{inf} can be approximated by the atmospheric pressure due to the large difference between the air and water density (2). According to the dynamic condition on the dry-wet interface S_{inf}, the total pressure of the air on the dry sand side of S_{inf} is controlled by the total fluid pressure on the wet sand side, which itself is affected by the height of the first peak wave: if the sliding speed is the same, a higher peak will increase the hydro-static pressure on the wet sand side of S_{inf}, and thus increase the total fluid pressure in the wet sand (see Fig. 8(b) and Fig. 9(b))

and the total pressure of the air in the dry sand through the dynamic boundary condition on the wet-dry interface.

An increased air pressure in the dry sand increases the general buoyancy in the dry sand as shown in Fig. 11: the air pressure on the interface between the air and the dry sand can be approximated by the atmospheric pressure; therefore, an increased general buoyancy acting on the sand reduces the stresses in the solid phase, which in turn reduces the stress between the sand and the bed τ_b, leading to a reduced resistance from the slope to the sliding mass, F_f^* (see Fig. 10). As a result, a higher air pressure in the dry sand tends to increase the speed of the sliding sand. An increased sliding speed may increase the dynamic pressure in the water, and thus further increase the air pressure in the sand. This action-reaction process between the air pressure in the dry sand and the slide speed stops when the waves have left the granular front.

4.3 Effect of grain size on the speed of granular front

As shown in Table 3, both the experiment and simulation revealed that the speed of the granular front increases with decreasing grain size. The experimental results of Jop et al. (2006) seemed to imply that smaller dry particles sliding on a slope had less inertia and thus experienced less friction, resulting in a faster sliding speed. To confirm this, two additional laboratory tests and numerical simulations were conducted using the very coarse sand and the fine sand in the absence of the water, and the results are presented in Appendix 5. The results show that (i) in the absence of the water, the fine sand and the very coarse sand have almost the same sliding speed and (ii) the fine sand and the very coarse sand have similar frictional forces. Therefore, the rheological effect on the sliding speed due to the particle size, as suggested by Jop et al. (2006), is insignificant. As a result, the finer sand slides faster only in the presence of water, and the explanation for this must lie in the interaction between water and sand.

The forces affecting the motion of the sand include: gravitational force, the drag force between the sand and the fluid, the general buoyancy acting on the sand, solid-phase stresses (which parameterize the interactions among sand grains), and the frictional force between the sand and the slope. The speed of the granular front is expected to be directly controlled mainly by the forces acting on the dry sand; this is because (i) the volume of the wet sand is negligible compared to the volume of the dry sand, and (ii) the fluid pressure and drag force acting on the wet sand by the water tend to decelerate the motion of the wet sand.

For the forces the solid phase experiences, the frictional force in the solid phase is one order-of-magnitude larger than the general buoyancy, which itself is several times larger than the drag between the fluid and the sand (Fig. 11). The change of the frictional force caused by the grain size is about 0.1, the change of the general buoyancy caused by the grain size is about 0.09, and the change of the drag caused by the grain size is about 0.02. Therefore, the effect

of the grain size on the drag force can not be the major cause of the change of the sliding speed caused by the grain size. The major causes are (i) the general buoyancy acting on the dry sand and (ii) the frictional force between the sand and the slope.

A relatively high air pressure in the dry fine sand discussed in Section 4.2 results in an increase in the general buoyancy acting on the sand (see the force F_b^* in Fig. 11), which can reduce the sediment-phase stresses since they are parameterizations of the normal and tangential forces among the sand grains; as a result, the fine sand experiences less internal friction and is more easy to flow down the slope compared to the very coarse sand. The reduction of sediment-phase stresses in the fine sand also reduces the force between the sand and the slope (which was roughened by the very coarse sand in the experiment), and thus makes the fine sand to slide slightly faster than the very coarse sand.

4.4 Effect of grain size on the wave height

As shown in Fig. 7, both the experiment and the simulation have shown that the wave height increases with decreasing grain size. The higher wave height for the fine sand may be understood by (i) the lower penetration rate of fine sand and (ii) the faster sliding speed of the fine sand.

As discussed in Section 4.1, the volume of the wet sand is purely controlled by the penetration of water into the sand and reducing grain size decreases the penetration rate; therefore, the volume of wet sand for the fine sand will be smaller than that for the very coarse sand, and thus can not be a direct reason for the higher wave height observed for the fine sand. As a result, the total volume of the displaced water should be controlled mainly by the volume of the dry sand in the region bounded by S_{inf} and the still water level, which increases with decreasing grain size.

As Lee and Huang (2021) has pointed out, the wave height is correlated with the thickness of the granular front at the moment when the first wave is about to leave the influence of the granular front ($t = 0.26\,\mathrm{s}$). Before that moment, the wave is a forced wave whose celerity is the same as the sliding speed and whose height is proportional to the thickness of the granular front. Lee and Huang (2021) studied only one grain size (the very coarse sand) and defined the thickness of the granular front by averaging the thicknesses corresponding to the five neighboring highest points on the contour line of $c = 0.5$. As shown in Fig. 6(a) or Fig. 8(a), at $t = 0.26\,\mathrm{s}$ the interface between the dry and wet sand S_{inf} for the very coarse sand intersect with the contour line of $c = 0.5$ at the location where $\delta_{0.5}$ is defined, meaning that $s_0 \approx \delta_{0.5}$ in Lee and Huang (2021).

For the fine sand, however, the interface between the dry and wet sand S_{inf} is between the contour lines of $c = 0.5$ and $c = 0.1$ at the moment when the first wave is about to leave the granular front (see Fig. 9(a)). Therefore, it is more suitable to use the interface of the dry-wet sand S_{inf} instead of the

contour line of $c = 0.5$ to define the thickness of the granular front (which is essentially the thickness of the dry portion of the granular front) and discuss the displacement of the water above the granular front.

As shown in Table 3, decreasing the grain size increases s_0, the thickness of the dry portion of the granular front, and the slide generates a forced wave before $t \leq 0.26\,\mathrm{s}$. Therefore, the fine sand is expected to generate a larger wave height than the very coarse sand; this is because a forced wave generated by a slide has a height determined by the thickness of the dry-sand near the granular front s_0, which has a larger value for the fine sand.

An increasing sliding speed can increase the height of the waves generated (Fritz et al., 2004). In the present problem, the fine sand slides also faster than the very coarse sand, and thus is expected to generate a larger wave. The slow penetration of water into the dry sand is the initial cause of a higher wave height for the fine sand, and then this higher wave height can increase the air pressure on the dry sand side of the dry-wet surface, which in turn increase the sliding speed and thus the wave height.

4.5 Effects of grain size on drag force and penetration rate

In the numerical model, the drag between the fluid and solid phases is parameterized by the particle response time, which is proportional to the grain size squared (Lee and Huang, 2021). The inverse of the particle response time is loosely equivalent to a linear drag coefficient. The effects of the grain size on the drag is twofold: (i) a smaller grain size gives a smaller particle response time and thus has the tendency to increase the drag, and (ii) a smaller grain size can make the particle more easy to follow the flow of the fluid (Lee et al., 2015a,b), and thus has the tendency to reduce the relative velocity and thus the drag. Figs. 11(c) and (d) imply that the first among these two effects dominates the drag force as the fine sand experiences a larger drag force than the very coarse sand. Since the drag force is much smaller than the frictional force and the general buoyancy, the direct effect of the drag on the sliding speed can be ignored. However, the effect of the grain size on the penetration of water into the sand, which is related to the drag, cannot be ignored. A slower penetration rate is related to a larger drag. Reducing the grain size increases the drag and reduces the penetration rate.

4.6 Over-prediction of the thickness of the granular front and the height of the first wave

As shown in Fig. 6 and mentioned in Section 3.6, the present model over-predicts the thickness of the granular front and thus the wave height. This over-prediction is possibly caused by the formula adopted to compute the particle response time. For example, in low-concentration regions the expression for the particle response time was derived from the hindered settling velocity in a quiescent fluid (Richardson and Zaki, 1954). In quiescent conditions,

the particles have special micro-structure arrangements (Yin and Koch, 2007). However, the particle's arrangement in non-quiescent conditions may be different. It seems that existing formulas for the particle response time all underestimate the particle response time for fine sand, leading to the following two consequences: (i) the drag is over-predicted and thus the penetration rate is under-predicted, and (ii) the sand in the model is over responsive to the vortex near the granular front, and thus more suspension. The first results in an over-prediction of the thickness of granular front s_0 and thus the wave height, and the second leads to an over-prediction of $\delta_{0.1}$ (the vertical distance between the contour line of $c = 0.1$ and the slope). The over-predictions of the thickness of the granular front and the wave height become more obvious for the fine sand possibly because the particle response time adopted in our model is proportional to the sand diameter squared.

4.7 Evaluation of the model performance

The performance of the present model in simulating the impulse waves can be measured using either Normalized Root-Mean-Square Error (NRMSE) or the skill value (or index of agreement) proposed by Willmott (1981). The NRMSE is defined as the root-mean-square error normalized by the difference between the maximum and minimum observed surface elevations. The NRMSE and skill values for all four cases are included in Table 4. The NRMSE is 10% for the very coarse sand and 15% for the fine sand. The skill values for all cases are larger than 93%.

Table 4: NRMSE and skill values for Cases 1-4

Case	NRMSE	skill
1	0.10	0.96
2	0.11	0.96
3	0.14	0.93
4	0.15	0.93

The performance of the present multi-phase model is not inferior to others reported in the literature. The differences between the measured and simulated peak amplitudes for the present model are 10 % for d=1.2 mm and 30 % for d=0.2 mm. Kim et al. (2019) used FLOW3D and TSUNAMI3D to simulate the waves generated by landslides of coarse granular particles (d=1.5 mm). They reported that the differences between the measured and simulated peak amplitudes could be 57% for TSUNAMI3D and 75% for FLOW3D.

4.8 Scale effects

Experiments are usually designed based on Froude similarity where the sand and the density and viscosity of the water are not scaled in model tests. As

a result, the following dimensionless parameters may result in scale effects: (i) Reynolds number for viscous effects, (ii) Weber number for surface tension effects. The air and water can be regarded as imcompressible fluids in the present problem.

Two Reynolds numbers can be defined: a grain Reynolds number (Kesseler et al., 2020) for viscous effects between sand grains and water, and a bulk Reynolds number (Heller et al., 2008) for viscous effects on the propagation of impulse waves. Following Heller et al. (2008), the bulk Reynolds number can be defined by $Re_h = u_w h/\nu_f$ with $u_w = \sqrt{gh}$ as a scale for the velocity of the water motion. Following Kesseler et al. (2020), the grain Reynolds number can be defined by $Re_d = u_s d/\nu_f$ with $u_s = \sqrt{2gh_f}$ (h_f is the drop height) as a scale for the velocity of granular material at impact. The Weber number can be defined by $We = \rho_w g h^2/\sigma_w$ with ρ_w being the density of water and σ_w the surface tension (Heller et al., 2008).

For the present study, $Re_h = 1.64 \times 10^5$ and $We = 26,716$. According to Heller et al. (2008), the surface tension can be neglected when $We > 5,000$, and the water viscosity has an effect on wave attenuation only if $Re_h < 3 \times 10^5$. In the real world, $h \gg 0.14$ cm; therefore, the viscose effects on wave attenuation is not expected to be significant.

For dry landslides, Kesseler et al. (2020) shows the sliding velocity is sensitive to Re_d when $10^2 < Re_d < 10^3$. In this study, $O(Re_d) = 100$ if $h_f = H_i$ is used. Therefore, the small facility used in this study is expected to result in some significant scale effect mainly for the sediment dynamics.

5 Conclusions

This experimental and numerical study examined the effects of grain size on the impulse waves generated by subaerial landslides. A multi-phase flow model was used to simulate the subaerial landslides and the resulting waves. Both the measured and simulated results have suggested that the finer sand can have a faster sliding speed and generate larger waves. The simulated results have showed: (i) the fine sand can yield a higher pore pressure in the sand, which can increase the general buoyancy the sand experiences and thus reduce the solid-phase stresses and the frictional force between the sand and the slope, explaining why the fine sand slides faster; (ii) a lower infiltrating rate of the fine sand leads to a thicker granular front, which explains why the fine sand generates a larger wave. The multi-phase flow model slightly over-predicts the thickness of the granular front and the height of the first wave, and it is hypothesised that a better model for the particle response time may correct these over-predictions.

Acknowledgements

This is SOEST contribution No. 112237.

Funding

The material is based on work supported by the Ministry of Science and Technology, Taiwan [MOST 110-2636-E-110-010] and the U.S. National Science Foundation under the grant No. 1706938. Any opinions, findings, and conclusions or recommendations expressed in this material are those of the author(s) and do not necessarily reflect the views of the National Science Foundation.

Availability of data and material

The datasets for the the current study are available in the Mendeley repository (doi:10.17632/6zm6jj97yf.1).

Appendix. Measured and simulated results for Cases 5 and 6

To help understand the role of the water-sand interaction, additional tank tests were conducted using the very coarse sand and the fine sand in the absence of water in the tank. Multi-phase flow simulations were also performed for these two cases to obtain information about the forces experienced by the sand in the absence of water.

Fig. 12(a) shows the air-sand interfaces measured at $t = 0.26$ and 0.6 s for the very coarse sand and the fine sand. It can be seen that the air-sand interfaces for these two grain sizes are almost identical at both $t = 0.26$ and 0.6 s, suggesting that the sliding process is not affected by the grain sizes and the grain-size effects on the sliding process is related to the water-sand interaction.

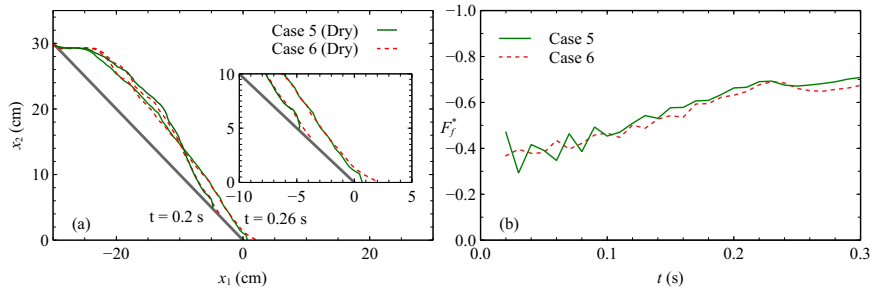

Fig. 12: (a): The air-sand interfaces measured at $t = 0.2$ s and 0.26 s in the absence of the water body for the very coarse sand (Case 5) and the fine sand (Case 6). (b): The simulated time series of the frictional force between the dry sand and the slope for the very coarse sand (Case 5) and the fine sand (Case 6).

Fig. 12(b) shows the simulated frictional forces F_f^* for the very coarse sand and the fine sand. The grain size does not have a significant effect on

the frictional force between the dry sand and the surface of the slope. The fluctuation of the frictional forces in the initial stage has to do with the initial adjustment. After starting the simulation, the sand in the numerical model will need to go through an initial adjustment in the initial stage of the simulation ($t < 0.02\,\mathrm{s}$). During this initial adjustment period, the initial pressure and volume concentration of the solid phase adjust themselves to incorporate the effects of the sand weight. It can be concluded that the grain size has no noticeable effects on the frictional force between the sand and the rough surface of the slope.

As for the general buoyancy and the drag force (figures are not included here), they are both less than 0.2% of the maximum frictional force.

References

Abadie SM, Harris JC, Grilli ST, Fabre R (2012) Numerical modeling of tsunami waves generated by the flank collapse of the Cumbre Vieja Volcano (La Palma, Canary Islands): Tsunami source and near field effects. J Geophys Res 117(5):1–26

Artoni R, Santomaso A (2014) Effective wall slip in chutes and channels: experiments and discrete element simulations. Granul Matter 16(3):377–382

Bellotti G, Romano A (2017) Wavenumber-frequency analysis of landslide-generated tsunamis at a conical island. Part II: EOF and modal analysis. Coastal Eng 128:84–91

Bougouin A, Paris R, Roche O (2020) Impact of fluidized granular flows into water: Implications for tsunamis generated by pyroclastic flows. J Geophys Res 125(5):e2019JB018954

Bradski G, Kaehler A (2008) Learning OpenCV: Computer vision with the OpenCV library. O'Reilly Media, Inc.

Chen F, Heller V, Briganti R (2020) Numerical modelling of tsunamis generated by iceberg calving validated with large-scale laboratory experiments. Advances in Water Resources 142:103647

Cheng S, Zeng J, Liu H (2020) A comprehensive review of the worldwide existing tsunami databases. J Earthq Tsunami 14(05):2040003

Das BM (2013) Principles of Geotechnical Engineering, vol 53. Cengage Learning, Stamford

Di Risio M, De Girolamo P, Bellotti G, Panizzo A, Aristodemo F, Molfetta MG, Petrillo AF (2009) Landslide-generated tsunamis runup at the coast of a conical island: New physical model experiments. J Geophys Res 114(1):1–16

Engelund (1953) On the laminar and turbulent flows of ground water through homogeneous sand. Danish Academy of Technical Sciences, Copenhagen

Evans SG (1989) The 1946 Mount Colonel Foster rock avalanche and associated displacement wave, Vancouver Island, British Columbia. Can Geothch J 26(3):447–452

Evers FM, Hager WH, Boes RM (2019) Spatial impulse wave generation and propagation. J Waterw Port, Coast and Ocean Eng 145(3):04019011
Ferziger JH, Peric M (2002) Computational methods for fluid dynamics. Springer, Berlin
Forterre Y, Pouliquen O (2003) Long-surface-wave instability in dense granular flows. J Fluid Mech 486:21–50
Fritz HM, Hager WH, Minor HE (2003) Landslide generated impulse waves. 2. Hydrodynamic impact craters. Exp Fluids 35(6):520–532
Fritz HM, Hager WH, Minor HE (2004) Near field characteristics of landslide generated impulse waves. J Waterw Port Coast Ocean Eng 130(6):287–302
Grilli ST, Shelby M, Kimmoun O, Dupont G, Nicolsky D, Ma G, Kirby JT, Shi F (2017) Modeling coastal tsunami hazard from submarine mass failures: effect of slide rheology, experimental validation, and case studies off the US East Coast. Nat Hazards 86(1):353–391
Heller V, Hager WH (2010) Impulse product parameter in landslide generated impulse waves. Journal of Waterway, Port, Coastal, and Ocean Engineering 136(3):145–155
Heller V, Spinneken J (2013) Improved landslide-tsunami prediction: Effects of block model parameters and slide model. J Geophys Res 118(3):1489–1507
Heller V, Spinneken J (2015) On the effect of the water body geometry on landslide-tsunamis: Physical insight from laboratory tests and 2D to 3D wave parameter transformation. Coast Eng 104:113–134
Heller V, Hager WH, Minor HE (2008) Scale effects in subaerial landslide generated impulse waves. Experiments in Fluids 44:691–703
Higuera P, Lara J, Losada I (2014) Three-dimensional interaction of waves and porous coastal structures using OpenFOAM. Part I: Formulation and validation. Coast Eng 83:243–258
Hsu T, Sakakiyama T, Liu P (2002) A numerical model for wave motions and turbulence flows in front of a composite breakwater. Coast Eng 46:25–50
Huang B, Yin Y, Liu G, Wang S, Chen X, Huo Z (2012) Analysis of waves generated by Gongjiafang landslide in Wu Gorge, three Gorges reservoir, on November 23, 2008. Landslides 9(3):395–405
Huang B, Yin Y, Chen X, Liu G, Wang S, Jiang Z (2014) Experimental modeling of tsunamis generated by subaerial landslides: Two case studies of the Three Gorges Reservoir, China. Environ Earth Sci 71(9):3813–3825
Huang B, Zhang Q, Wang C Jianand Luo, Chen X, Chen L (2020) Experimental study on impulse waves generated by gravitational collapse of rectangular granular piles. Phys Fluids 32(3):033301
Jop P, Forterre Y, Pouliquen O (2006) A constitutive law for dense granular flows. Nature 441(7094):727–730
Kamphuis J, Bowering R (1972) Impulse waves generated by landslides. In: Proceedings of 12th ICCE, Reston, pp 195–214
Kesseler M, Heller V, Turnbull B (2020) Grain reynolds number scale effects in dry granular slides. J Geophys Res 125(1):e2019JF005347
Kim GB, Cheng W, Sunny R, Horrillo J, McFall B, Mohammed F, Fritz H, Beget J, Kowalik Z (2019) Three dimensional landslide generated tsunamis:

Numerical and physical model comparisons. Landslides 17:1–17
Lee CH, Huang Z (2018) A two-phase flow model for submarine granular flows: With an application to collapse of deeply-submerged granular columns. Adv Water Res 115:286–300
Lee CH, Huang Z (2021) Multi-phase flow simulation of impulsive waves generated by a sub-aerial granular landslide on an erodible slope. Landslides 18:881–895
Lee CH, Huang Z, Chiew YM (2015a) A three-dimensional continuum model incorporating static and kinetic effects for granular flows with applications to collapse of a two-dimensional granular column. Phys Fluids 27(11):113303
Lee CH, Huang Z, Chiew YM (2015b) A multi-scale turbulent dispersion model for dilute flows with suspended sediment. Adv Water Res 79:18–34
Lee CH, Xu C, Huang Z (2019) A three-phase flow simulation of local scour caused by a submerged wall jet with a water-air interface. Adv Water Resour 129:373–384
Lindstrøm EK (2016) Waves generated by subaerial slides with various porosities. Coast Eng 116:170–179
Liu PLF, Wu TR, Raichlen F, Synolakis CE, Borrero JC (2005) Runup and rundown generated by three-dimensional sliding masses. J Fluid Mech 536:107–144
Lynett P, Liu PL (2005) A numerical study of the run-up generated by three-dimensional landslides. J Geophys Res 110:1–16
Løvholt F, Pedersen G, Harbitz CB, Glimsdal S, Kim J (2015) On the characteristics of landslide tsunamis. Philos Trans A Math Phys Eng Sci 373(2053):20140376
Ma G, Kirby JT, Hsu TJ, Shi F (2015) A two-layer granular landslide model for tsunami wave generation: Theory and computation. Ocean Model 93:40–55
McFall B, Mohammed F, Fritz H, Liu Y (2018) Laboratory experiments on three-dimensional deformable granular landslides on planar and conical slopes. Landslides 15:1713–1730
McFall BC, Fritz HM (2016) Physical modelling of tsunamis generated by three-dimensional deformable granular landslides on planar and conical island slopes. P Roy Soc A-Math Phy 472(2188):20160052
Miller DJ (1960) Giant waves in Lituya bay, Alaska. US Government Printing Office, Washington, DC
Mohammed F, Fritz HM (2012) Physical modeling of tsunamis generated by three- dimensional deformable granular landslides. J Geophys Res 117:C11015
Müller L (1964) The rock slide in the Vajont Valley. Rock Mech Eng Geol 2:148–212
Mulligan RP, Take WA (2017) On the transfer of momentum from a granular landslide to a water wave. Coast Eng 125:16–22
Noda E (1970) Water waves generated by landslides. J Waterw Harb Coast Eng Div 96(4):835–855
Ouriemi M, Aussillous P, Guazzelli E, Guazzelli É (2009) Sediment dynamics. Part 1. Bed-load transport by laminar shearing flows. J Fluid Mech 636:295–

319
Pilvar M, Pouraghniaei MJ, Shakibaeinia A (2019) Two-dimensional subaerial, submerged, and transitional granular slides. Phys Fluids 31:113303
Rauter M, Hoße L, Mulligan RP, Take WA, Løvholt F (2021) Numerical simulation of impulse wave generation by idealized landslides with OpenFOAM. Coast Eng 165(November 2020):103815
Richardson JF, Zaki WN (1954) Sedimentation and fluidisation: Part I. Chem Eng Res Des 32:S82–S100
Robbe-Saule M, Morize C, Henaff R, Bertho Y, Sauret A, Gondret P (2021) Experimental investigation of tsunami waves generated by granular collapse into water. J Fluid Mech 907:A11
Romano A, Lara JL, Barajas G, Di Paolo B, Bellotti G, Di Risio M, Losada IJ, De Girolamo P (2020) Tsunamis generated by submerged landslides: Numerical analysis of the near-field wave characteristics. J Geophys Res 125(7):1–26
Ruffini G, Heller V, Briganti R (2019) Numerical modelling of landslide-tsunami propagation in a wide range of idealised water body geometries. Coast Eng 153(May):103518
Shi C, An Y, Wu Q, Liu Q, Cao Z (2016) Numerical simulation of landslide-generated waves using a soil-water coupling smoothed particle hydrodynamics model. Adv Water Resour 92:130–141
Si P, Shi H, Yu X (2018) A general numerical model for surface waves generated by granular material intruding into a water body. Coastal Eng 142(September):42–51
Vacondio R, Mignosa P, Pagani S (2013) 3D SPH numerical simulation of the wave generated by the Vajont rockslide. Adv Water Resour 59:146–156
Viroulet S, Cébron D, Kimmoun O, Kharif C (2013a) Shallow water waves generated by subaerial solid landslides. Geophys J Int 193(2):747–762
Viroulet S, Sauret A, Kimmoun O, Kharif C (2013b) Granular collapse into water: Toward tsunami landslides. J Vis 16(3):189–191
Walder JS, Watts P, Sorensen OE, Janssen K (2003) Tsunamis generated by subaerial mass flows. J Geophys Res 108(B5):2236
Wang B, Yao L, Zhao H, Zhang C (2020) Composite impulse waves triggered by a combined earthquake and landslide. J Earthq Tsunami 14(01):2050002
Willmott C (1981) On the validation of models. Phys Geogr 2:184–194
Yavari-Ramshe S, Ataie-Ashtiani B (2015) A rigorous finite volume model to simulate subaerial and submarine landslide-generated waves. Landslides 14(1):203–221
Yin X, Koch DL (2007) Hindered settling velocity and microstructure in suspensions of solid spheres with moderate Reynolds numbers. Phys Fluids 19(9):093302
Yu ML, Lee CH (2019) Multi-phase-flow modeling of underwater landslides on an inclined plane and consequently generated waves. Adv Water Resour 133:103421
Zhao T, Utili S, Crosta GB (2016) Rockslide and Impulse Wave Modelling in the Vajont Reservoir by DEM-CFD Analyses. Rock Mech Rock Eng

49(6):2437–2456
Zitti G, Ancey C, Postacchini M, Brocchini M (2016) Impulse waves generated by snow avalanches: Momentum and energy transfer to a water body. J Geophys Res 121(12):2399–2423
Zweifel A, Hager WH, Minor HE (2006) Plane impulse waves in reservoirs. J Waterw Port Coastal Ocean Eng 132:358–368